Effects of Droop Based Fast Frequency Response on Rotor Angle Stability During System Wide Active Power Deficits

Zaichun Zhang, *Student Member, IEEE*, and Robin Preece, *Senior Member, IEEE*

***Abstract*—The effects of fast frequency response (FFR) on rotor angle stability have predominately been established by examining the oscillatory behavior of synchronous generators (SGs). What remains largely unexamined, however, is the effect that FFR has on the angle separation and power transfer between SGs. This paper systematically examines the evolution of the angle separation and power transfer between SGs during FFR provision in the context of frequency containment events. Droop based FFR schemes, which are popular and effective in practical systems, are analyzed. This research investigates how the location of the initiating system wide active power deficit, the location of resources providing FFR, and the delays associated with FFR provision all impact rotor angle stability. The key results are obtained using a modified IEEE 39-bus system and further verified using a reduced-order dynamic Great Britain system model. The results show that the angle separation and power transfer between SGs decrease when power deficits occur in areas with extensive generation sources which, conversely, implies that angle stability deteriorates if power deficits occur near load centers. A key finding is that providing the FFR at locations closest to the source of the initial power deficit does not always enhance angle stability, and sometimes has a significant adverse effect. The effect that FFR delays have on rotor angle stability is explained, highlighting the necessity to carefully consider and design FFR provision timing, particularly in areas with diminishing levels of inertia.**

***Index Terms*—Delay, fast frequency response, power transfer, rotor angle separation, rotor angle stability.**

I. Introduction

TO ACHIEVE net zero targets, conventional synchronous generators (SGs) are progressively being displaced by converter interfaced generation (CIG) sources. Unlike SGs, CIGs do not inherently release or absorb synchronously connected kinetic energy (i.e., *inertia*) to reduce any frequency deviations following disturbances. The ability of the power system to retain its frequency stability thus diminishes as the CIG proliferates. Relying only on conventional primary frequency control schemes to contain frequency deviations will prove prohibitive due to slow responding processes and high operational costs. Fast frequency response (FFR) provides an attractive and often highly cost-effective alternative to mitigate the deterioration in frequency stability. Years of research have demonstrated the applicability of providing FFR from various technologies and devices [1]. Both *droop based* response and *virtual inertia* response can be provided, dependent on the control schemes applied [2].

Given the potential for injecting fast, controllable active power at any point within power networks, recent years have seen a growing research interest in the effects of FFR on *rotor angle stability*. Rotor angle stability refers to the ability of interconnected SGs in a power system to maintain synchronism during nominal operating conditions as well as following disturbances [3]. It depends not only on the equilibrium between the mechanical torque and electrical torque of each SG but also on the angle separation between SGs (or groups of SGs). Accordingly, previous research within this field can be classified into two thematic areas: (1) effects of FFR on oscillatory stability, and (2) effects of FFR on angular separation between SGs.

Widespread research has been conducted into the FFR effects on oscillatory stability, with most of the focus being on the inhibition of SG oscillation using virtual inertia (VI). The effects of VI on small-signal rotor angle stability have been studied extensively, as in [4], [5], [6]. Also, the optimal allocation of VI in the system has been a topic of much interest, as in [7], [8], [9], [10]. To inhibit SG oscillation against large system perturbations (for example short circuit faults), a multitude of VI controllers are designed, as in [11], [12], [13], [14]. There are also studies concerning the effects of droop based FFR, as in [15], [16], [17]. These studies, however, focus more on developing FFR implementation strategies that inhibit oscillatory FFR injection instead of stabilizing SG oscillation.

In contrast, the effect that FFR can have on the angular separation between SGs has received much less attention. The studies within this area are concerned with whether the power system can retain synchronism following a *system wide active power deficit* (underfrequency disturbance event). The underlying stability issues are characterized by large angular differences between areas and substantial power transfer across AC inter-area ties. Studies [18] and [19] highlight that the relative spatial location of the initial power deficit and the subsequent FFR provision plays an important role in influencing system

Manuscript received 4 July 2023; revised 23 November 2023; accepted 28 January 2024. Date of publication 9 February 2024; date of current version 21 August 2024. Paper no. TPWRS-01028-2023. *(Corresponding author: Zaichun Zhang.)*

The authors are with the Department of Electrical and Electronic Engineering, The University of Manchester, M13 9PL Manchester, U.K. (e-mail: zaichun.zhang@manchester.ac.uk; robin.preece@manchester.ac.uk).

Color versions of one or more figures in this article are available at https://doi.org/10.1109/TPWRS.2024.3364532.

Digital Object Identifier 10.1109/TPWRS.2024.3364532

0885-8950 © 2024 IEEE. Personal use is permitted, but republication/redistribution requires IEEE permission.
See https://www.ieee.org/publications/rights/index.html for more information.

Authorized licensed use limited to: FH Dortmund. Downloaded on November 22,2024 at 11:39:02 UTC from IEEE Xplore. Restrictions apply.

stability. It is a reported view that providing FFR further away from the area or network node where the initial power deficit occurs leads to a degradation of angle stability [18], [19]. As a result, prioritizing the FFR resources closest to the power deficit location has commonly been used as a design aim for FFR control schemes, as in [20], [21].

Numerous FFR allocation schemes, controller designs, and implementation strategies have been shown to effectively stabilize system oscillation. However, the effects of the inherent and/or intentional delays incurred during the initiation of the FFR services have rarely been considered in previous research, which may limit the applicability of those methods in practical systems. Although providing FFR close to the source of the initial power deficit has been recommended to enhance angle stability, this conclusion is drawn from analysis based on a single disturbance location and may not be generalizable to other disturbance locations. The mechanism through which the angle separation between SGs evolves during the FFR service delivery has not been fully understood and requires clarification.

This paper presents a comprehensive investigation into the effects of FFR on rotor angle stability during system wide active power deficits. Droop based FFR schemes are widely implemented worldwide [22]; whereas derivative based schemes, such as inertia-like services, still face numerous implementation challenges that require resolving [23]. Thus, droop based FFR schemes are implemented in this paper. However, it should be noted that the conclusions drawn from the paper continue to be applicable when a derivative controller is incorporated, as demonstrated in Appendix A. Unlike the previous research that has typically focused on only one aspect of the FFR impacts, both the oscillatory behavior of SGs and the angle separation between SGs are examined in this paper. Also, many consider measurement delays and associated communication latency as major contributors to FFR delays [22]; this paper, however, adopts a holistic view, considering all potential sources of FFR delay in a practical environment. Variations in power deficit location, FFR placement, FFR delay, system- and regional-wide inertia are studied to establish the effect on system stability. Analytical and numerical (simulation based) approaches are used to illustrate the findings. The key results are obtained using a modified IEEE 39-bus system and further verified using a reduced-order dynamic Great Britain (GB) system model.

The main contributions of this paper are:

1) An analytical explanation of how power deficit location, FFR placement, and FFR delay affect angle stability.
2) A novel understanding of how the FFR placement in relation to the power deficit location affects angle stability.
3) A thorough investigation into the impact of FFR delays on rotor angle stability.
4) The identification of the critical SGs with respect to FFR-induced angular instability following a system wide active power deficit event.

II. Theoretical Background

This research is primarily focused on the ability of the power system to maintain synchronism when subjected to a major active power deficit that requires frequency support from droop based FFR. The corresponding electromechanical dynamics involve large system frequency excursions, significant SG oscillations, alongside substantial active power interchange between areas. The time scale of interest is 3–5 s following the initial power deficit, during which the FFR can be fully operating, whereas the SG governor control that operates the turbine working fluid input valve has not had time to initiate.

A. Rotor Dynamics During Frequency Containment Events

In this study, the oscillatory behavior of SGs refers to the periodic transition of rotor acceleration and deceleration during frequency containment events. This is studied by examining the *net torque imbalance* imposed on the rotor in conjunction with the *equal area criterion* (EAC), which is based on the law of conservation of energy [24]. Following a major active power deficit (ΔP), the power imbalance is shared among all the connected SGs within the system. The amount of load that each SG initially picks up depends on its *electrical distance* (i.e., the Thévenin impedance) from the location where the power deficit occurs [24]. The SG nearest to the power deficit will experience the largest load pick up. The pick up results in an instantaneous increase in the electrical power demand placed on the SG (P_e), which consequently causes an increase in the electrical torque (τ_e) imposed on the rotor given by (1) where ω is the SG angular speed. Due to the slow acting turbine governor control, the mechanical power (P_m) provided by the turbine remains roughly unchanged following the pick up. The mechanical torque (τ_m) applied by the turbine hence keeps constant in (1). The resulting negative net torque imbalance (τ_{net}) imposed on the rotor in (1) leads to rotor deceleration, governed by the *swing equation* in (2), where $\Delta\omega$ and ω_{syn} refer to the angular speed deviation and the synchronous angular speed respectively, H is the inertia constant of the SG, S is the SG rating, and M is the SG angular momentum, which is equivalent to the synchronous inertial energy stored within the SG [24].

$$\tau_m = \frac{P_m}{\omega}; \tau_e = \frac{P_e}{\omega}; \tau_{net} = \tau_m - \tau_e \tag{1}$$

$$\frac{d}{dt}\Delta\omega = \frac{d}{dt}(\omega - \omega_{syn}) = \frac{\tau_{net}}{2HS} = \frac{\tau_{net}}{M} \tag{2}$$

$$\frac{d}{dt}\delta = \Delta\omega \tag{3}$$

Both M and τ_{net} play a major role in determining rotor dynamics. These factors not only determine the change of frequency deviation that is experienced but also the angle divergence (δ) at a specific location as given by (3). In a multi-area network, not only does each area store a specific amount of inertia, but the initial τ_{net} experienced after the power deficit is also different. Locational variations in rotor speed deviations will hence be seen around the system, leading to active power interchange across AC inter-area ties and angular divergence between areas.

Following the initial pick up, rapid injections of power delivered by the FFR devices will propagate through the system and will be realized as a sudden decrease in τ_e on the rotor,

Authorized licensed use limited to: FH Dortmund. Downloaded on November 22,2024 at 11:39:02 UTC from IEEE Xplore. Restrictions apply.

TABLE I
CHANGES IN POWER TRANSFER UNDER DIFFERENT CONDITIONS

	Power Deficit Location	
FFR Placement	Sending end area	Receiving end area
Sending end area	(7a)	(7c)
Receiving end area	(7b)	(7d)

introducing an additional positive τ_{net} superimposed on the rotor oscillations. The SG nearest to the FFR injection will experience the largest FFR-induced additional τ_{net}. Any FFR action that changes the work done during acceleration (or deceleration) will affect the maximum angular divergence in either direction in the subsequent swings, governed by the EAC. Stability is maintained only if the kinetic energy gained during acceleration is fully absorbed by the work performed during deceleration.

B. Steady State Power Transfer and Angle Separation

Assuming all SGs remain in synchronism during the frequency containment events, they will rotate at approximately the same rate after a few rotor swings. At this stage, the FFR provides droop based steady state power injection, and the system frequency is stabilized to a new equilibrium (but not nominal frequency). The power flow across AC inter-area ties may be altered compared to the pre-event conditions, which contributes to variations in angular separation between areas.

For a general case, consider a sending end source $V_S = |V_S|\angle\theta_S$ transferring power to a receiving end source $V_R = |V_R|\angle\theta_R$ via a reactance X_L. The power P_S injected from the sending end area is described by the *power-angle characteristic* in (4). Assuming both sources are connected to strong AC grids and there are no network topological changes during the frequency containment process, P_S in (4) is hence a sine function only of the angle separation θ_{SR}. Rearranging (4) with θ_{SR} as the subject gives (5), where θ_{SR} is monotonically increasing with P_S. Any increase in P_S would increase θ_{SR}, and vice versa.

$$P_S = \frac{|V_S|\,|V_R|}{X_L} sin\left(\theta_S - \theta_R\right) = \frac{|V_S|\,|V_R|}{X_L} sin\theta_{SR} \tag{4}$$

$$\theta_{SR} = arcsin\left(P_S \Big/ \frac{|V_S|\,|V_R|}{X_L}\right) \tag{5}$$

The change in P_S is determined by three factors: (1) the power deficit location, (2) the FFR placement, and (3) the contribution of each area to the steady state power imbalance as given by (6) where ΔP_i is the share of i-th area or SG in meeting the power imbalance, M_i is the synchronous inertial energy stored within i-th area or SG, $\mathcal{G}$ is the total number of committed SG units within the system, and P_{imb} is the steady state power imbalance [24].

$$\Delta P_i = \frac{M_i}{\sum_{g=1}^{\mathcal{G}} M_g} P_{imb} \tag{6}$$

Table I summarizes the changes in P_S resulting from all possible combinations of power deficit and FFR locations, with further details provided in (7) and a derivation in Appendix B, where ΔP is the size of the initial power deficit, P_{FFR} is the amount of power delivered by the FFR devices, M_S and M_R represent the amount of regional inertia of the sending end and the receiving end areas respectively. These points are of significance and will be used later in the analysis into the locational impact of the power deficit and FFR provision in Section IV-A.

$$\Delta P_S = (\Delta P - P_{FFR}) - \frac{M_S}{M_S + M_R}(\Delta P - P_{FFR}) \tag{7a}$$

$$\Delta P_S = \Delta P - \frac{M_S}{M_S + M_R}(\Delta P - P_{FFR}) \tag{7b}$$

$$\Delta P_S = P_{FFR} + \frac{M_S}{M_S + M_R}(\Delta P - P_{FFR}) \tag{7c}$$

$$\Delta P_S = \frac{M_S}{M_S + M_R}(\Delta P - P_{FFR}) \tag{7d}$$

III. METHODOLOGY

To enable a systematic investigation, both an analytical approach and a numerical approach (simulation based) are employed in this research. Analytical analysis is conducted to explain the mechanisms that govern the rotor angle divergence of an SG during frequency containment events. To facilitate the analysis, a *single machine infinite bus* (SMIB) system is used as the test network. The results obtained will be used to propose preliminary findings. A numerical approach is used to test the preliminary findings drawn from the analytical studies and to extend the investigation using large, practically scaled multi-machine systems. As the fundamental frequency dynamics are of interest, the power system, and all included components, are modeled using a positive sequence phasor representation. Simulations are performed at the electromechanical level, assuming the three phases are balanced and all CIGs operate under strong system conditions, characterized by a high short-circuit ratio.

A. Variations in System Initiation and Network Topology

To enable the generalizability of the results, a scenario-based analysis is conducted during the investigation. This includes variations in power deficit location, FFR placement, and FFR delay. For multi-machine systems, system performance under varying levels of system- and regional-wide inertia is also examined. To establish the robustness of the key findings to topological and system dynamics alterations, simulation based studies are performed on two large practical systems.

B. Power System Modeling

In this subsection, models are presented for system components including SGs, supplementary SG controls, loads, CIGs, and transmission lines. It is noted, and fully appreciated, that simplified models will be used to support the analytical discussion, whereas high-fidelity representation will be considered in simulation based studies to generalize the obtained findings.

For numerical simulations, 5th and 6th-order models [24] are used to represent salient-pole and round-rotor SGs respectively.

Authorized licensed use limited to: FH Dortmund. Downloaded on November 22,2024 at 11:39:02 UTC from IEEE Xplore. Restrictions apply.

Whereas, for analytical analysis, the SG is represented by the *classical model* (a transient emf E' behind a transient reactance X'_d), with assumptions consistent with [24]. An ideal voltage source is used to represent the infinite bus in the SMIB system. Supplementary SG controls, including excitation system, power system stabilizer, and turbine governor system, are included for numerical simulations, while they are neglected in analytical studies. System loads are modeled using the polynomial ZIP model [3] for numerical simulations, whereas constant power loads are considered for analytical analysis. For numerical simulations, CIGs are represented by generic phasor-based (average-value) models [23], incorporating decoupled inner current control based on vector control strategy. Converter synchronization is achieved using a generic synchronous reference frame phase locked loop (SRF-PLL) [25]. Given the great flexibility and controllability, grid scale battery energy storage systems (BESSs) are considered as the FFR provider in this research. Other CIGs, if included in studies, do not provide any frequency containment services. For FFR control, an additional SRF-PLL is incorporated into the BESS, operating with slower dynamics compared to the converter synchronization PLL (varying PLL parameters have a negligible impact on the results obtained as demonstrated in Appendix C). For analytical analysis, current sources are incorporated to represent CIGs (and the FFR devices) [8]. Regarding transmission lines, a lumped parameter model and the common π-representation [3] are considered for numerical simulations, whereas both the resistance and shunt susceptance of the lines are neglected for analytical analysis.

C. Active Power Deficit Event Modeling

The disconnection of a CIG is implemented as the initial power deficit. In this way, the pre- and post-event synchronous inertial energy available in the system is identical. This ensures that results are not affected by changes in inertia, which could be the case if SG tripping is implemented. For numerical simulations, the power deficit is sized to the most frequent power in-feed loss of the practical systems. For analytical analysis, it is sized to 14% of the total generation. This allows reasonably large speed deviations of the single SG without the system losing synchronism solely due to such an event.

D. Fast Frequency Response (FFR) Modeling

To ensure clarity during FFR implementation, this research classifies the FFR into two categories based on volume specification [26]: *static* (switched or pre-determined) FFR, and *dynamic* (or continuous) FFR. The former typically deploys its total available volume, giving a fixed, single sized offset to the initial power deficit. Conversely, dynamic FFR provides a portion of its total available volume but is continuously sensitive to frequency deviation and acts to control its provision.

For analytical studies, the FFR is modeled for conceptualization purposes only and implemented as a static, fast ramp-up response. The initial rapid linear power delivery can be justified by considering it is inversely proportional to the initial drop of SG's $\Delta\omega$ (which is similarly approximately linear) [27]. The FFR capacity is sized to 50% of the initial power deficit. For numerical simulations, dynamic FFR implementation is considered. The FFR is deployed based on local signals, providing frequency nadir services. The supplementary frequency control alongside the outer active power control loop is displayed in Fig. 1.

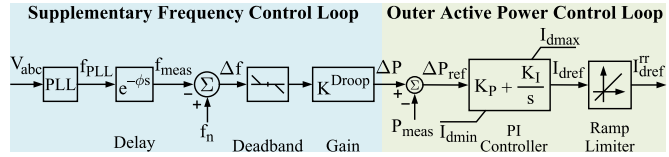

Fig. 1. BESS active power-frequency control.

The input of the frequency controller is the frequency deviation (Δf), which is the difference between nominal frequency (f_n) and locally measured frequency (f_{meas}) at the point of common coupling. The FFR delay is modeled as a standard delay function as given by $F(s) = e^{-\phi s}$ in the Laplace domain, added into the estimated frequency signal output of the PLL (f_{PLL}). This representation, unlike a first-order filter [15], [28], allows for exact, discrete variations in FFR delay, making it more effective for examining its impact. A dead band is implemented to prevent excessive operation of FFR around f_n. The proportional controller is represented as a droop gain K^{Droop}. The output signal (ΔP) is sent as the setpoint to the outer control which is a proportional-integral (PI) controller. The outer control is subjected to a ramp limiter to represent the BESS converter power ramp limitations. The dead band size, K^{Droop}, and FFR capacity are specified based on grid codes and will be elaborated further in Section IV. The ramp rate of FFR is set at 4 pu/s with respect to the converter rating, according to the technical requirements for providing the Dynamic Containment (DC) service procured by the GB National Grid Electricity System Operator (NGESO) [29].

1) Delay of FFR Provision: The summation of four different sources of delay incurred during the initiation of the FFR services in a practical environment is considered cumulatively as the FFR delay. This includes (1) the time taken for frequency event detection, (2) measurement delays incurred by signal processing and communication, (3) intentional FFR service delivery delays specified by system operators (SOs), and (4) operational delays of the controllers. As local input signals are selected, the associated measurement delays are marginal. The operational delays of the controllers are negligible for the time scale of interest. Given that existing technologies can deliver FFR in a few milliseconds [22], [27], the minimum FFR delay considered in this research is 50 ms. Although some SOs favor fast response, NGESO specifically advocates a delayed response, typically between 250 to 500 ms after a frequency event occurs, to avoid spurious operation of the FFR devices [29]. Further, frequency event detection typically takes around 250 ms in practice [20]. Accordingly, FFR delays up to 500 ms after the initial power deficit are considered and hence, FFR delays examined in this research lie in the range [50, 500] ms.

2) Network Distribution of FFR Provision: Both highly distributed and relatively concentrated FFR provision could improve frequency nadir [28]. Also, FFR provision at a single

Authorized licensed use limited to: FH Dortmund. Downloaded on November 22,2024 at 11:39:02 UTC from IEEE Xplore. Restrictions apply.

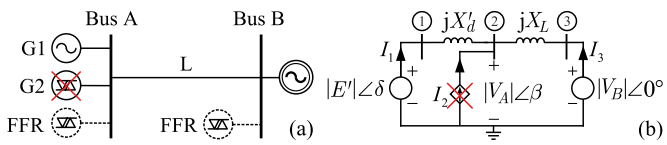

Fig. 2. SMIB system: (a) single line diagram, and (b) equivalent circuit.

location is used successfully in [27] to improve frequency nadir in a multi-machine system. In this research, regional concentrated FFR provision is considered for numerical simulations. Single-location FFR is implemented for analytical studies.

E. Threshold for Angle Instability

For the SMIB system, the infinite bus provides the reference that defines the spatial angular position of the rotor. Values of δ beyond 180° are considered unstable [24]. For multi-machine systems, the maximum angular difference between any two SGs at the same instant time during system transients ($\Delta\delta_{\max}$) is used as an indicator of angle stability. Values of $\Delta\delta_{\max}$ beyond 240° are considered unstable [30].

IV. Application and Results

In this section, the details of the application of the methodology outlined in Section III are presented. As a recap, three test networks are used to perform the analysis in this paper. The first network is a SMIB system which is used for analytical analysis. The results obtained will be used to propose preliminary findings. The second network is a modified IEEE 39-bus system model which is used to test the proposed findings and to further develop the investigation. The third network is a reduced-order dynamic GB system model, which is used to verify that the key findings can be generalized. Modeling and simulations are performed using DIgSILENT PowerFactory 2021.

A. Analytical Analysis of the SMIB System

The SMIB system is shown in Fig. 2(a), with the equivalent circuit displayed in Fig. 2(b). The generator bus (Bus A) and the infinite bus (Bus B) are connected via a single AC transmission line (L). The disconnection of a static generator (G2) at Bus A is always used to unbalance the system. The FFR is delivered from another static generator, with two possible injection locations in the system, Bus A and Bus B. Throughout the analysis, the angle difference between E' and the voltage of Bus B (V_B) is denoted as δ; the angle difference between the voltage of Bus A (V_A) and V_B is denoted as β; the angle difference between E' and V_A is denoted as α. The steady state power injections from G1, G2, and the FFR device are denoted as P_{G1}, P_{G2}, and $0.5P_{G2}$, respectively.

Two scenarios described below will be analyzed. For simplicity, a constant load at Bus A is only introduced for *Scenario 2*. As the disconnection of G2 is always applied at Bus A, in practical terms, *Scenario 1* might represent a situation where a power deficit occurs in a *distant generation zone* that initially exports power to a large network through a long transmission corridor. Conversely, *Scenario 2* represents a power deficit event occurring in a remote *load center* that initially imports power from a large network.

- *Scenario 1:* the system initially operates with power transfer from Bus A to Bus B.
- *Scenario 2:* the system initially operates with power transfer from Bus B to Bus A.

1) Steady State Analysis: This analysis aims to investigate how P_{G1}–δ curve changes on the (δ, P) plane under four different operating conditions: (1) *Pre-event*, (2) *Post-event*, (3) *Post-event with FFR at Bus A*, and (4) *Post-event with FFR at Bus B*. Due to physical constraints, it is assumed that the SG primary response has not yet had time to operate for the time scale of interest and hence, the mechanical power P_m provided by G1's turbine remains fixed. As will be shown, the change in the steady state power transfer from Bus A to Bus B induced by the initial power deficit (and potentially the subsequent FFR provision) drives the differences in these operating conditions, which consequently leads to different system performance with respect to rotor angle stability. For clarity, the discussion will begin with *Scenario 1*.

From (4) and (5), the values of α and β (and hence δ) can be calculated as given by (8), where P_{G1} is the power flowing via X'_d, and P_A^{inj} is the power transferred from Bus A to Bus B via X_L.

$$\delta = \alpha + \beta = arcsin\left(P_{G1} \Big/ \frac{|E'|\,|V_A|}{X'_d}\right) + arcsin\left(P_A^{inj} \Big/ \frac{|V_A|\,|V_B|}{X_L}\right) \tag{8}$$

Assuming the static generators are connected to a strong AC grid (Bus A in this case), the values of both $|E'|\,|V_A|/X'_d$ and $|V_A||V_B|/X_L$ in (8) remain fixed. Governed by (6), the share of G1 in meeting the power imbalance for all operating conditions is zero as the infinite bus (Bus B in this case) will almost entirely cover the power imbalance. P_{G1} hence remains constant and is always equal to P_m. Conversely, P_A^{inj} can be altered as outlined in Table I. As a result, the change in the steady state value of δ is fully governed by the variation in β (i.e., P_A^{inj}) as indicated by (9) where α_0 is the initial steady state value of the angle difference between E' and V_A, the value of $|V_A||V_B|/X_L$ is denoted as $const.$ for simplicity.

$$\delta = \alpha_0 + arcsin\left(P_A^{inj} \Big/ const.\right);$$
$$\alpha_0 = arcsin\left(P_m \Big/ \frac{|E'|\,|V_A|}{X'_d}\right) \tag{9}$$

On the (α, P) plane, the initial equilibrium point of the $P_{G1}(\alpha)$ curve – derived from (4), is denoted as (α_0, P_m). As the magnitude of E', V_A, and X'_d remains unchanged, the magnitude of the $P_{G1}(\alpha)$ curve remains constant under the four operating conditions. As governed by (9), what changes is the position of the equilibrium point (α_0, P_m) on the (δ, P) plane, depending on the variation of β (or P_A^{inj}). As P_m remains constant, the change in (α_0, P_m) essentially means a translation of the $P_{G1}(\alpha)$

Authorized licensed use limited to: FH Dortmund. Downloaded on November 22,2024 at 11:39:02 UTC from IEEE Xplore. Restrictions apply.

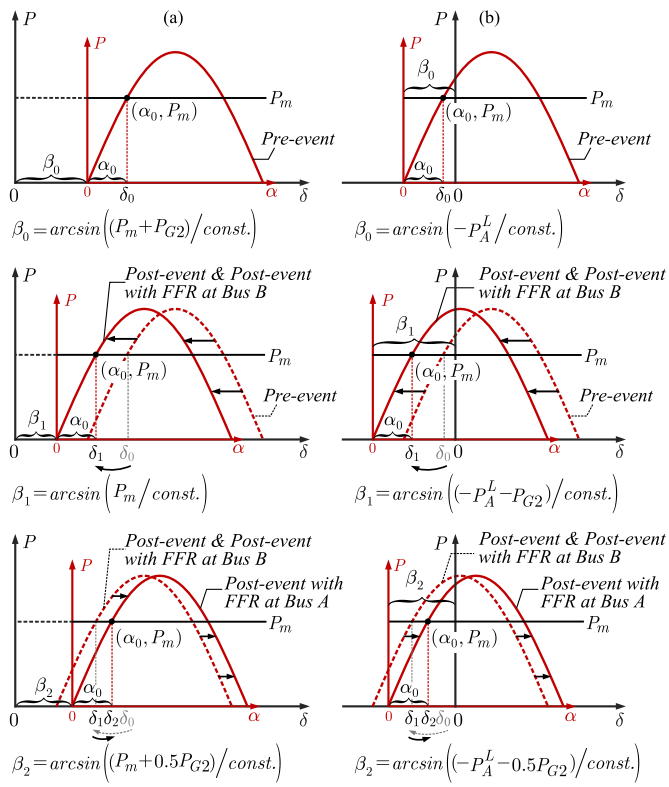

Fig. 3. Shift of $P_{G1}(\alpha)$ curve on the (δ, P) plane under different operating conditions: (a) *Scenario 1*, (b) *Scenario 2* (N.B. due to the intrinsic interaction through β, the α and δ axes are effectively superimposed. The shifts of the $P_{G1}(\alpha)$ curve are hence indicative of the changes in δ).

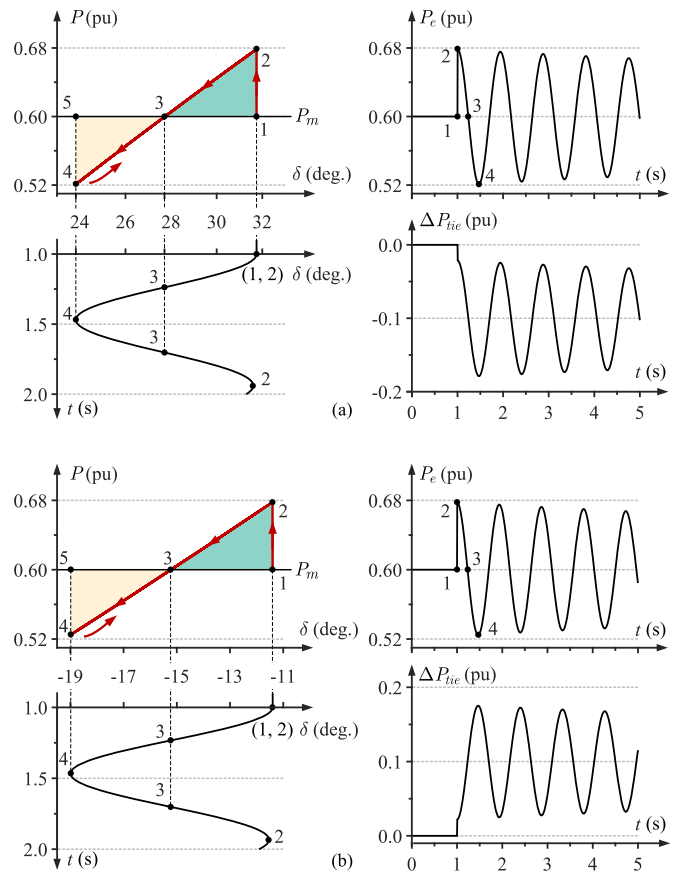

Fig. 4. Power deficit analysis: (a) *Scenario 1*, (b) *Scenario 2*. $|E'| = 1.1$ pu, $|V_B| = 1.0$ pu, $X'_d = 0.2$ pu, $X_L = 1.08$ pu, $P_m = 0.6$ pu, $P_{G2} = 0.1$ pu.

curve in a given horizontal direction on the (δ, P) plane. This is illustrated in Fig. 3(a). The analytical expression of P_{G1} in (11) further supports this idea (see Appendix D.) – the shift of the $P_{G1}(\alpha)$ curve on the (δ, P) plane is fundamentally governed by the variation of β.

For the *Pre-event* condition, $P_A^{inj} = P_m + P_{G2}$. For both the *Post-event* and the *Post-event with FFR at Bus B* conditions, P_A^{inj} is reduced by P_{G2} governed by (7). The $P_{G1}(\alpha)$ curve thus translates to the left with respect to the *Pre-event* condition as shown in Fig. 3(a), indicating an *increase* in angular stability margin of the whole system. For the *Post-event with FFR at Bus A* condition, $P_A^{inj} = P_m + 0.5P_{G2}$. The $P_{G1}(\alpha)$ curve thus translates to the right with respect to both the *Post-event* and the *Post-event with FFR at Bus B* conditions as shown in Fig. 3(a), indicating a *decrease* in the stability margin of the system.

Although the current analysis focuses on *Scenario 1*, the mechanism through which the $P_{G1}(\alpha)$ curve shifts on the (δ, P) plane continues to be applicable to *Scenario 2*, as shown in Fig. 3(b). Note that in this case the absolute values of the angles (β and δ) are negative with respect to the infinite bus, and the *Pre-event* $P_{G1}(\alpha)$ curve is shifted to the left by a constant value corresponding to the net load at Bus A.

Interestingly, the shifts of the $P_{G1}(\alpha)$ curve lead to opposite conclusions as compared to *Scenario 1*. For the *Pre-event* condition, $P_A^{inj} = -P_A^L$ where P_A^L is the net load at Bus A. For both the *Post-event* and the *Post-event with FFR at Bus B* conditions, the tie line L is additionally loaded by P_{G2} as governed by (7). Thus, the $P_{G1}(\alpha)$ curve translates to the left with respect to the *Pre-event* condition as shown in Fig. 3(b), indicating a *decrease* in the angular stability margin of the system. For the *Post-event with FFR at Bus A* condition, the additional load on L is partially offset by the FFR ($0.5P_{G2}$). The $P_{G1}(\alpha)$ curve thus translates to the right with respect to both the *Post-event* and the *Post-event with FFR at Bus B* conditions as shown in Fig. 3(b), indicating an *increase* in angular stability margin of the whole system.

The previous analysis explains how the power deficit location and the FFR placement affect rotor angle stability under steady state conditions. When the power deficit occurs in the distant generation zone (*Scenario 1*), the angular stability margin of the whole system increases; providing the FFR close to the power deficit location diminishes the stability margin. Conversely, the angular stability margin decreases when the power deficit occurs in remote load centers (*Scenario 2*); providing the FFR close to the power deficit location however alleviates the resultant angle stability concerns.

The time evolution of δ during frequency containment events is governed by the shift of the $P_{G1}(\alpha)$ curve on the (δ, P) plane, which is elaborated on in the following analysis.

2) Impact of Power Deficit Location: A comparative analysis is given for *Scenarios* 1 and 2. Fig. 4 displays the transient responses. To enhance clarity, only the relevant portions of the

Authorized licensed use limited to: FH Dortmund. Downloaded on November 22,2024 at 11:39:02 UTC from IEEE Xplore. Restrictions apply.

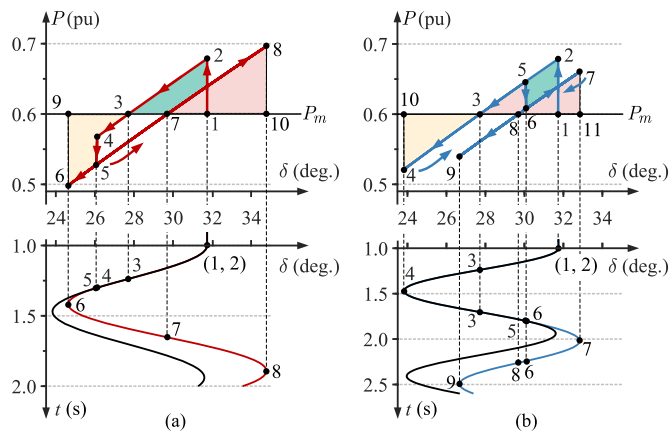

Fig. 5. FFR delay analysis: (a) $T_d = 300$ ms, and (b) $T_d = 800$ ms.

$P_{G1}(\alpha)$ curves that depict the movement of the system operating point are presented. The electrical power output of G1 (P_e) and the change in power transfer on the tie line L (ΔP_{tie}) are also given to help illustrate the effect.

The curve 1–2–3–4–3–2 in Fig. 4(a) depicts how the system responds to a power deficit that occurs in the distant generation zone. Prior to the event, the system operates at point 1, i.e., $(\delta_0,\ P_m)$ of the *Pre-event* curve in Fig. 3(a). Point 3 is the equilibrium point that determines the position of the *Post-event* curve, i.e., $(\delta_1,\ P_m)$ in Fig. 3(a). The initial load pick up of G1 is depicted by curve 1–2. As the rotor experiences negative τ_{net}, it starts to decelerate, causing the operating point to move from 2 to 3. During this motion, G1's electrical power output P_e decreases, resulting in reduced power transfer through L and hence, decreased angular separation δ. Considering the EAC, the rotor will continually oscillate between points 2 and 4 around point 3 in the absence of any damping.

For *Scenario 2*, the movement of the system operating point on the $(\delta,\ P)$ plane shares similar characteristics with *Scenario 1* as shown in Fig. 4(b). The equilibrium points, 1 and 3, correspond to (δ_0, P_m) and (δ_1, P_m) in Fig. 3(b) respectively. Unlike *Scenario 1*, increased power transfer through L and angular separation δ are seen during the initial swing of G1. Although the threshold for angle instability is respected, the increase in the maximum variation of the instantaneous power on L is virtually twice the magnitude of the power deficit. Such significant power swings might exceed transmission limits in practical systems, potentially leading to system separation or unintentional islanding.

3) Impact of FFR Delay: For clarity, the discussion is limited to *Scenario 1*, with the FFR always injected at Bus A, being adjacent to G1. A comparative analysis is given for two different FFR delays (300 and 800 ms). Fig. 5 displays the system responses. Also included for comparison is the rotor angle divergence for the *Post-event* condition (shown in black).

The curve 1–2–3–4–5–6–5–7–8 in Fig. 5(a) depicts how the rotor swings will be increased by the FFR if it is delivered when the rotor is accelerating – in this case with a 300 ms delay. As before, point 3 determines the position of the *Post-event* curve in Fig. 3(a). Point 7 is the equilibrium point that determines the position of the *Post-event with FFR at Bus A* curve, i.e., (δ_2, P_m) in Fig. 3(a). The FFR injection starts when the system operates at point 4 – the rotor is experiencing positive τ_{net}. The FFR further increases the positive τ_{net} on the rotor, pushing the operating point to move from 4 to 5. The rotor continues to accelerate until it stops at point 6, such that the area (3–4–5–6–9) equals the area (1–2–3). Considering the EAC, the rotor will then swing back and continually oscillate between points 6 and 8 around point 7. Area (7–8–10) is larger than area (1–2–3), indicating that the kinetic energy acquired during the rotor acceleration is increased as a result of the FFR provision. This explains the subsequent larger δ swing following the FFR.

The curve 1–2–3–4–3–5–6–7–6–8–9 in Fig. 5(b) depicts how the rotor swings will be reduced by the FFR that is delivered when the rotor is decelerating – here with a delay of 800 ms. In this case, point 8 determines the position of the *Post-event with FFR at Bus A* curve, i.e., (δ_2, P_m) in Fig. 3(a). The delivery of the FFR starts at point 5 – the rotor is experiencing negative τ_{net}. The FFR-induced positive τ_{net} counteracts the rotor deceleration such that the operating point moves along the curve 5–6. Due to the momentum the rotor continues to decelerate until it stops at point 7, such that the area (3–5–6–7–11) equals the area (3–4–10). As the area (7–8–11) is smaller than the area (1–2–3), a smaller magnitude of the subsequent δ swing is observed.

4) Analytical Findings: The mechanism explaining how power deficit location, FFR placement, and FFR delay affect rotor angle stability of a SMIB system has been presented. This is completed by analyzing the changes in the system angular stability margin under steady state conditions and the resulting system dynamic performance over time. An increased angular margin reduces the likelihood of the system reaching instability boundary (180°) during transient angle swings, thereby enhancing overall angle stability; conversely, a reduced margin makes the SG angular divergence more likely to approach 180° during angle swings, thereby degrading the overall angle stability. Accordingly, three findings from the analytical studies are proposed. They will be tested and further extended by performing phasor based simulations on larger test systems.

1) Impact of power deficit location – If the power deficit occurs in distant generation zones, then the system angular difference will initially reduce after the disturbance. This will typically improve angle stability. Conversely, if the power deficit occurs close to load centers, then the system angular difference will initially increase. This will typically degrade angle stability.
2) Impact of FFR placement – FFR is more likely to degrade angle stability if it is injected in distant generation zones, even for cases when the initial power deficit occurs in the same area. Conversely, FFR is more likely to improve angle stability if it is injected close to load centers, no matter where the initial power deficit occurs.
3) Impact of FFR delay – FFR injections delivered in the same time frame as nearby SG speed increases will reinforce the rotor swings and degrade angle stability. Conversely, injections that coincide with the speed reductions

Authorized licensed use limited to: FH Dortmund. Downloaded on November 22,2024 at 11:39:02 UTC from IEEE Xplore. Restrictions apply.

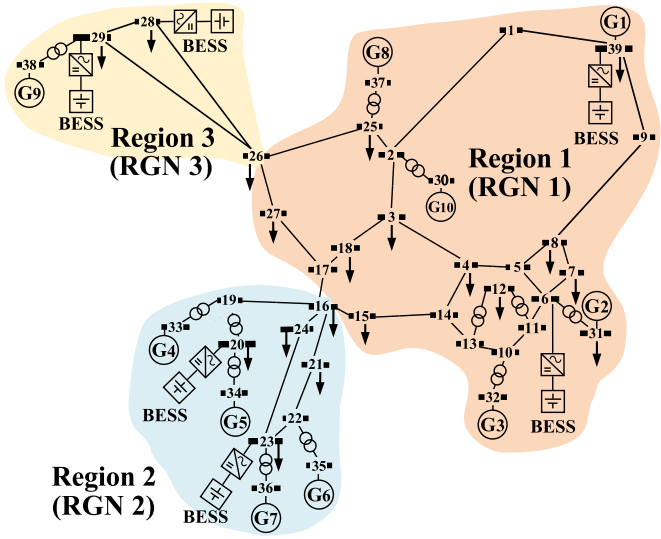

Fig. 6. Scaled single-line diagram of IEEE 10-machine, 39-bus system.

of nearby SGs will reduce rotor swings and improve angle stability.

B. Application of the Modified IEEE 39-Bus System

Fig. 6 displays a graph of the IEEE 39-bus system which accounts for the physical length of lines (based on impedance). To enable the analysis under low inertia operating conditions, the system is modified based on the assumptions made in [27], wherein it was calibrated to represent the Irish power system. To facilitate the analysis, the system is split into three regions by considering the locations of load centers and the network topology. Load centers are concentrated in RGNs 1 and 2. RGN 3 can hence be considered as a distant generation zone. RGN 1 represents a meshed network; both RGNs 2 and 3 represent more radial networks. During steady state operation, G1 (in RGN 1) and G9 (in RGN 3) operate with the lowest and highest relative angle displacement respectively.

The concentrated FFR is provided by two identical BESSs in each region of the system. Six BESSs are therefore implemented which will be operated in pairs during each simulation. Further studies (not included for brevity) have shown that changes in BESS placement in a specific region will only affect the numerical results achieved, but not the general trend or mechanisms observed. The BESS model in PowerFactory is implemented to represent the dynamics of the FFR devices. The FFR scheme is designed to maintain the system frequency above 49.5 Hz during power deficit events. To create worst operating conditions, the dead band is sized at ± 0.2 Hz, which is the largest acceptable dead band for providing FFR services in the Irish system [31]. A K^{Droop} value of 0.6% is thus implemented. The power deficit is always sized to 430 MW, which is currently being considered as the most likely and severe single power in-feed loss in the Irish system [27].

To conduct a comprehensive analysis, three scenarios described in Table II are used.

TABLE II
EXAMPLE SCENARIO PARAMETERS FOR THE IEEE 39-BUS SYSTEM

	Synchronous Inertial Energy (GVA·s)				FFR
	System	RGN 1	RGN 2	RGN 3	(MW)
Base case	21.5	11.6	7.2	2.7	360
Reduced Inertia	17.5	9.5	5.8	2.2	500
Regional Inertia	17.5	11.6	4.3	1.6	500

TABLE III
CASE STUDY NAMES: POWER DEFICIT LOCATION AND FFR PLACEMENT

	FFR in RGN 1	FFR in RGN 2	FFR in RGN 3
Event at bus 29	*Ev29_FFR1*	*Ev29_FFR2*	*Ev29_FFR3*
Event at bus 39	*Ev39_FFR1*	*Ev39_FFR2*	*Ev39_FFR3*

- *Base Case* Scenario: The system inertia is 21.5 GVA·s and the total capacity of FFR is sized to 360 MW [27].
- *Reduced Inertia* Scenario: This scenario is used to examine how the FFR-induced impacts change with reduced system inertia. The H values of all SGs are reduced by 20% from the *Base Case* scenario. The system inertia is 17.5 GVA·s, which is expected to be the lowest inertia floor of the Irish system in 2030 [32]. Due to declined system inertia, the FFR capacity is increased to 500 MW, matching the largest BESS capacity assumed in [27] for planning purposes in the Irish system.
- *Regional Inertia* Scenario: This scenario is used to ascertain FFR impacts in the presence of large differences in regional inertia. The H values of all SGs in RGNs 2 and 3 are reduced by 54% from the *Base Case* scenario, but the H values of all SGs in RGN 1 are the same as in the *Base Case* scenario.

1) Impact of Power Deficit Location and FFR Placement: Simulations are performed for the *Base Case* scenario. A comparative analysis is given for six cases outlined in Table III. The event at bus 29 represents a power deficit in the distant generation zone. Whereas the event at bus 39 is adjacent to the largest load in the system. Fig. 7 displays the system center of inertia (COI) frequency (f_{COI}) and the trajectories of $\Delta\delta_{max}$ during transients. The change in power transfer on two tie lines (L29-26 and L1-39) is also presented to help establish the effect. To avoid potential detrimental impact of longer delays, the FFR is always delayed by 50 ms.

After the event at bus 29, the power transfer through the two tie lines is considerably diminished, and the value of $\Delta\delta_{max}$ initially reduces. Conversely, the power flow through the two tie lines and the value of $\Delta\delta_{max}$ initially rise after the event at bus 39. These results align with the first finding: that system angular difference will initially reduce after a power deficit occurs in a distant generation zone, whereas a power deficit close to load centers makes the system more prone to angle stability issues.

Regarding the impact of FFR placement, the FFR in RGN 3 (shown in red) always leads to greater values of $\Delta\delta_{max}$ and increased tie line flows. Conversely, the FFR provision in

Authorized licensed use limited to: FH Dortmund. Downloaded on November 22,2024 at 11:39:02 UTC from IEEE Xplore. Restrictions apply.

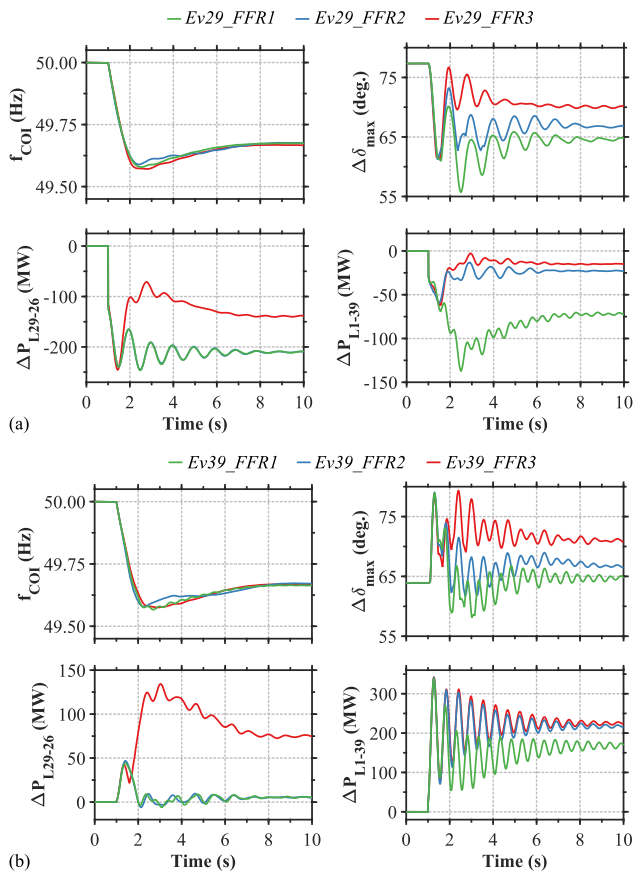

Fig. 7. Locational impact of power deficit and FFR provision: (a) power deficit event at bus 29, (b) power deficit event at bus 39.

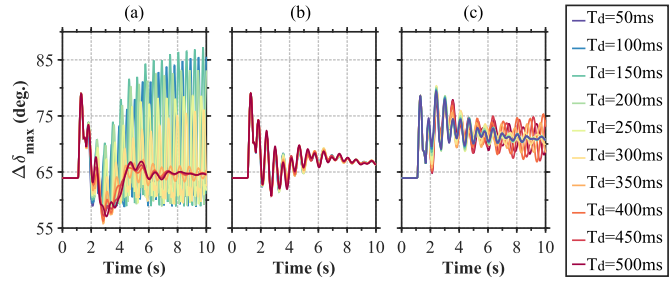

Fig. 8. Impact of FFR delay: (a) FFR at RGN 1, (b) FFR at RGN 2, (c) FFR at RGN 3 (N.B. $\Delta\delta_{\max}$ often occurs between G1 and G9 during transients; some lines are coincident as the y-axis is scaled to be comparable to other $\Delta\delta_{\max}$ plots).

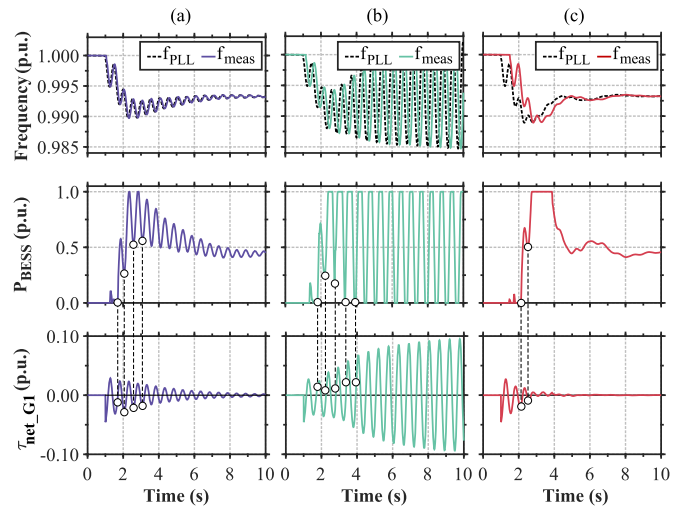

Fig. 9. Time series comparison: (a) $T_d = 50$ ms, (b) $T_d = 150$ ms, (c) $T_d = 500$ ms.

RGN 1 (shown in green) is consistently shown to result in smaller values of $\Delta\delta_{\max}$ and reduced tie line flows whilst improving frequency nadir. These results are consistent with the earlier observations, thereby further supporting the second finding: that FFR is more likely to degrade angle stability if it is injected in distant generation zones, even when the power deficit occurs in the same area (see *Ev29_FFR3*). Conversely, providing the FFR close to load centers minimizes power transfer and angle separation no matter where the power deficit occurs. This finding reveals that the previously reported view that angle stability is improved when FFR is located within the same network region as the initial power deficit is not always true and is more likely correct in situations where the power deficit occurs near load centers (see *Ev39_FFR1*).

Another finding to emerge from Fig. 7 is that angle stability is most likely to be degraded when the power deficit occurs near load centers and the subsequent FFR is provided in the distant generation zone (see *Ev39_FFR3*). This observation has practical implications as it provides some explanation as to why South Australia (SA) separated from Victoria (VIC) in the 2018 Australia blackout [33]. Initially, SA was exporting power to VIC. VIC experienced a power deficit due to the islanding of Queensland. As a result, the outgoing power from SA to VIC was suddenly increased and angle stability was degraded. The FFR was injected in SA (Homsdale), introducing additional power transfer from SA to VIC, further exacerbating the degradation of angle stability.

2) Impact of FFR Delay: Again, simulations are performed for the *Base Case* scenario. The power deficit is always applied at bus 39. The analysis is given for ten discrete FFR delays (50 to 500 ms in 50 ms time steps) at the three possible FFR provision regions – in total thirty separate operating scenarios.

Fig. 8 presents the trajectories of $\Delta\delta_{\max}$ during transients. It shows that in some cases the system experiences growing angle oscillations with delayed FFR provision in RGNs 1 and 3. Whereas the system always remains stable when providing the FFR in RGN 2. Additionally, the FFR delay that leads to instability varies with the FFR injection location. For example, consider a 150 ms FFR delay (shown in blue), providing the FFR in RGN 1 leads to instability, whereas the system remains stable if such an FFR is provided in RGN 3.

An inspection of the cause reveals that the instability stems from local oscillatory instability incurred by the FFR delay, as shown in Fig. 9. This comparison is generated for three FFR delays (50, 150, and 500 ms) with FFR located in RGN 1. These delays lead to stable, unstable, and stable system operations respectively, providing indicative results across the entire spectrum of delays considered. Focus is paid to the power output

Authorized licensed use limited to: FH Dortmund. Downloaded on November 22,2024 at 11:39:02 UTC from IEEE Xplore. Restrictions apply.

from the BESS at bus 39 (P_{BESS}) and the net torque imbalance of G1 (τ_{net_G1}) during frequency containment events. f_{PLL} and f_{meas} of the FFR control (see Fig. 1) are also presented to help illustrate the effect.

Fig. 9(b) shows that the initial oscillation of f_{PLL} is input into the FFR control with a delay of 150 ms, giving rise to the initial oscillation of P_{BESS}. Closer inspection of P_{BESS} and τ_{net_G1} shows that every fast and large injection of power coincides with the time when G1 experiences positive torque imbalance. Consequently this leads to unstable oscillations of G1, governed by the EAC. Whereas when the FFR is injected with a delay of 50 ms or 500 ms, the system remains stable despite the fact that P_{BESS} contains oscillations, as shown in Fig. 9(a) and (c). This is because the initial injections of power are always delivered within the time frame when τ_{net_G1} is negative, reducing the swing of τ_{net_G1}. These results are consistent with the previous observations and analysis, the third proposed finding is hence confirmed.

Further analysis by the authors (not included for brevity) reveals that the instability shown in Fig. 8(c) is attributed to unstable oscillation of G9 in the presence of delayed FFR provision. The absence of instability when providing the FFR in RGN 2 is because FFR injections are always delivered in the same time frame as the nearby SGs speed decreases. Due to variations in regional frequency, the local signal input for the FFR controller is different. This explains how the impact of FFR delay is strongly linked to the FFR location.

Again, the results in Fig. 8(a) challenge the previously reported view that angle stability is improved when the FFR response is located near the source of the power deficit. Delayed FFR provision may lead to local oscillatory instability.

3) Identification of Critical Generators: Considering all the analyses presented, G1 and G9 are considered critical with respect to the FFR-induced angle instability, with G9 being the most critical generator (CG). The criticality can be attributed to the initial (steady state) angle displacement, and the network locations in relation to bulk generation and load centers. Prior to the power deficit, G1 and G9 operate with the lowest and highest relative angle displacement respectively. This means that the angular stability margins of the whole system would most likely be dominated by their angle swings during frequency containment events (as evidenced by $\Delta\delta_{\max}$ observations in Fig. 8). Delivering FFR adjacent to these SGs makes the system more prone to angle instability incurred by poorly considered or selected FFR delays. Providing FFR in distant generation zones always causes additional power transfer across AC inter-area ties, resulting in greater angular separation across the system (as shown in Fig. 7). Due to this and its highest steady state angle displacement, G9 becomes more critical. Similar conditions in other systems (i.e., when SGs operate at the largest relative rotor angle displacement during steady state) would likely result in similar criticality. The SG within areas that contain extensive generation sources is recognized as more critical.

4) Impact of Reduced System and Regional Inertia: Simulations are performed for all three scenarios given in Table II. To create worst case scenarios, the power deficit is applied at bus 39, and the FFR is provided in RGN 3 – being close to the most critical generator G9. The analysis is given for ten discrete FFR delays. Fig. 10 presents the trajectories of $\Delta\delta_{\max}$.

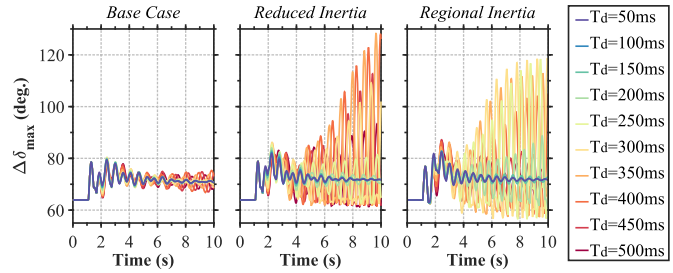

Fig. 10. Impact of reduced system- and regional-wide inertia (N.B. $\Delta\delta_{\max}$ often occurs between G1 and G9 during transients; some lines are coincident as the y-axis is scaled to be comparable to other $\Delta\delta_{\max}$ plots).

TABLE IV
RGN 3 INERTIA REDUCTION AND THE FIRST PROBLEMATIC FFR DELAY

	Inertia Reduction Pct.	1st Problematic FFR Delay
Base Case	N/A	350 ms
Reduced Inertia	20%	250 ms
Regional Inertia	54%	200 ms

From a system perspective, larger excursions of $\Delta\delta_{\max}$ are observed when the level of system inertia is reduced – the system becomes more vulnerable to FFR-induced angle stability degradation. This is consistent with the broad consensus that declined system inertia is likely to result in larger electromechanical oscillations during transient events.

From a regional perspective, as the inertia of RGN 3 diminishes (see Table II), the first FFR delay that leads to instability is advanced – earlier provision of FFR becomes more likely to degrade angle instability. Table IV provides the details. This highlights that FFR delay would be a trade-off between frequency stability and angle stability, and this is shown to be true for FFR provision areas that experience declined inertia.

C. Analysis on Great Britain System

A reduced-order model of the 2030 GB transmission network is used to verify that the key findings can be generalized. Fig. 11 shows the GB system which is a 29-node, 6-area network. Compared to the IEEE 39-bus system, the GB system not only exhibits a completely different network topology, but also operates at a high level of CIG penetration. Full network details are given in [34], with further explanations of the modifications detailed in [35]. The system initially operates with high flows of power transferring from Scottish generation zones (Areas 1 and 2) to English load centers (Areas 3 to 6). The Dynamic Containment (DC) service procured by NGESO is implemented into the BESS, intended to maintain the system frequency above 49.5 Hz after large power deficits [29]. Again, regional concentrated provision of FFR is considered, with BESSs evenly provided across each node within the area. The total capacity of FFR is 1,400 MW [29].

Authorized licensed use limited to: FH Dortmund. Downloaded on November 22,2024 at 11:39:02 UTC from IEEE Xplore. Restrictions apply.

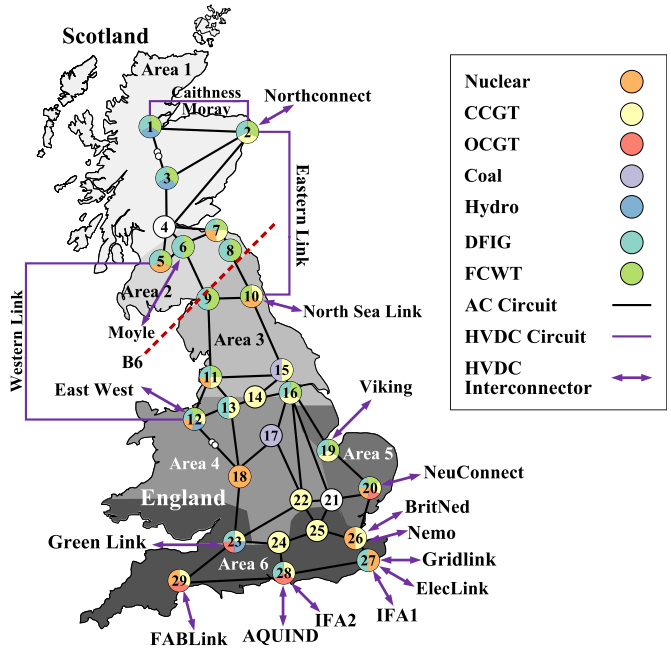

Fig. 11. Single-line diagram of 29-node, 6-area GB system in 2030.

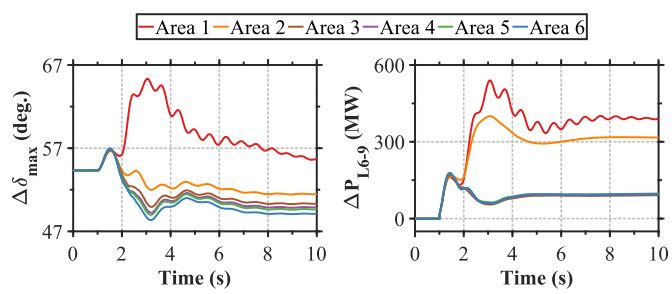

Fig. 12. Locational impact of power deficit and Dynamic Containment.

1) Critical Generator in the GB System: The CCGT unit at Node 2 (Area 1) and the hydro unit at Node 23 (Area 6) initially operate with the highest and lowest relative angle displacement respectively. The CCGT is considered most critical because it is located in the distant generation zones. The hydro unit is located in a heavily meshed area that contains load centers and is, hence, much less likely to lose synchronism during the frequency containment process.

2) Results and Verification: Two studies will be presented – the former verifying findings 1 and 2, and the latter verifying finding 3. The power deficit is always applied at Node 28 and sized to 1,320 MW, equivalent to the Normal Infeed Loss Risk for the GB system.

Firstly, simulations are performed for the six possible FFR provision areas. The minimum delivery time of the DC service is selected ($T_d = 250$ ms) to avoid potential instability incurred by longer delays. Fig. 12 displays the trajectories of $\Delta\delta_{\max}$, and the change in the power flow through the AC inter-area tie L6-9 (crosses the boundary B6).

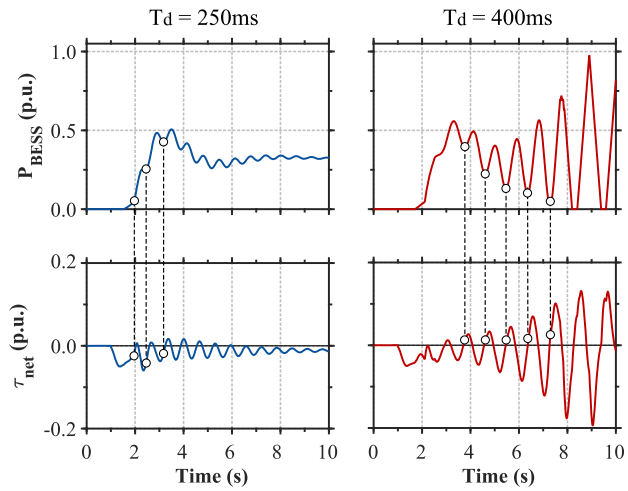

Fig. 13. Oscillatory rotor swings introduced by Dynamic Containment.

The value of $\Delta\delta_{\max}$ and the tie line flows rise after the initiation of the power deficit. The FFR injections in Areas 1 and 2 always lead to larger values of $\Delta\delta_{\max}$ and tie line flows, degrading angle stability, confirming the previous findings 1 and 2 about power deficit location, and FFR placement.

To verify the third finding, two different delays (250 and 400 ms) are considered, with the DC service always provided in Area 1 where the CG is located. Fig. 13 presents the responses. In the case with $T_d = 400$ ms, P_{BESS} has exacerbated the CG's τ_{net} oscillation as injections are delivered in the same time frame as CG speed increases. Eventually, the CG loses synchronism. Conversely, the system remains stable in the case with $T_d = 250$ ms as injections are delivered when the CG speed decreases. The third finding is hence confirmed.

V. Conclusion

This research provides a novel presentation of the link between fast frequency response (FFR) injections and rotor angle stability. Significantly, it reveals how power deficit location, FFR placement, and FFR delay affect the time evolution of angle divergence and power transfer between areas.

It has shown that areas with substantial loads are always preferable for FFR service provision without violating transmission limits or having a serious detrimental effect on angle stability. This in turn implies that additional power flows will be transferred across AC inter-area ties and angle stability is degraded following FFR injections when providing the FFR at distant areas that contain extensive generation sources. As the locational impact of power deficit and FFR provision heavily depends on the network locations of bulk generation and load centers, control schemes that prioritize the FFR resources closest to the initial power deficit location may provide very limited benefit to angle stability, and sometimes may adversely impact stability.

It has also shown that FFR delay results in a phase shift of the rapid power injections from the FFR devices and small variations in delays can cause transitions between stable and unstable

Authorized licensed use limited to: FH Dortmund. Downloaded on November 22,2024 at 11:39:02 UTC from IEEE Xplore. Restrictions apply.

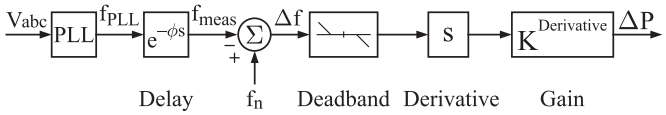

Fig. 14. Derivative based FFR controller.

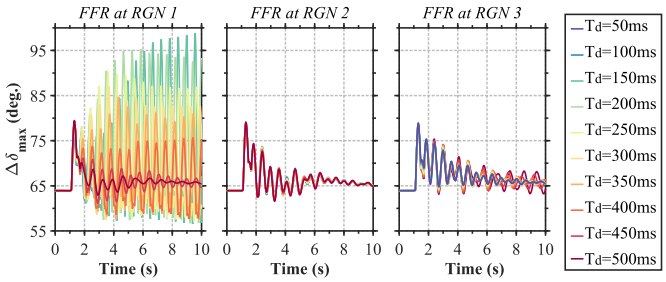

Fig. 15. Impact of FFR delay – derivative based FFR (N.B. $\Delta\delta_{\max}$ often occurs between G1 and G9 during transients; some lines are coincident as the y-axis is scaled to be comparable to other $\Delta\delta_{\max}$ plots).

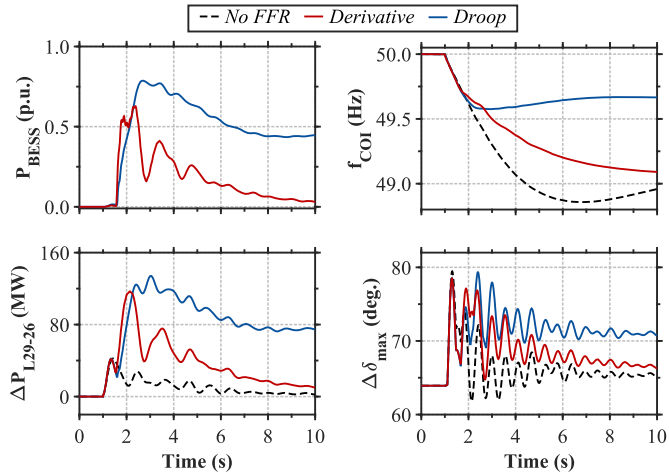

Fig. 16. Time domain comparison between droop and derivative FFR control.

system operations. Further, the effects of FFR delay exhibit locational variability due to variations in regional frequency. Although reduced FFR delays are advantageous to frequency containment they do not necessarily improve angle stability, especially in areas with diminishing levels of inertia. It is therefore crucial to carefully consider and design FFR delays in practical systems.

Appendix

A. Impact of Derivative Based FFR

To further enhance the conclusions drawn from the paper, two illustrative studies of the impact of *derivative based* FFR are presented. The former focuses on the impact of FFR delay, and the latter focuses on the impact of FFR placement. The modified IEEE 39-bus system (shown in Fig. 6) is used as the test network, with the simulations performed for the *Base case* scenario given in Table II. It is acknowledged that designing a derivative controller robust to practical considerations such as measurement noise is beyond the scope of this paper. Most importantly, as will be shown, the mechanisms pre-established in the paper remain valid when a derivative controller is incorporated.

The derivative FFR controller is shown in Fig. 14. A basic derivative function $F(s) = \mathrm{s}$ is used to enable inertial response emulation and the derivative is taken every time step of the simulation. A $K^{\text{Derivative}}$ value of 6 s is used, representing a typical inertia constant found in an SG or a wind turbine [24]. The dead band is sized at ± 0.2 Hz which is consistent with the original study setup. The power deficit is applied at bus 39 for all studies undertaken – creating worst case operating scenarios considering the detrimental impact of the power deficit near load centers.

1) Impact of FFR Delay: As with Section IV-B(2), the analysis is given for ten FFR delays at the three possible FFR provision regions, focusing on the trajectories of $\Delta\delta_{\max}$ during transients. Fig. 15 presents the results, which are consistent with the pre-established impact of FFR delay: that small changes in FFR delays can cause transitions between stable and unstable system operations and such impact exhibits locational variability.

2) Impact of FFR Placement: To highlight the key problem, a comparison between droop and derivative schemes is made. The FFR is always provided in RGN 3 – the distant generation zone in the network. To maximize the frequency stabilization benefits whilst avoiding potential angle instability incurred by longer delays, the FFR provision is delayed by just 50 ms. Fig. 16 displays the transient responses. Also included for comparison is the case with no FFR installed.

Looking at the final steady state settling values of the change in power transfer through L29-26 ($\Delta P_{\text{L29-26}}$) and $\Delta\delta_{\max}$, the *Derivative* case (shown in red) demonstrates a neutral effect compared to when no FFR is installed (shown in dashed black). Compared to the *Droop* case (shown in blue), however, it presents benefits regarding inhibition of large power transfer and angle separation between areas. This is because the rate of change of Δf settles to zero as the speed of the SGs settles. As such, P_{BESS} stabilizes to zero during steady state, not introducing additional power transfer between areas and further angular divergence.

Nevertheless, these benefits are dramatically reduced during transient response of the controller, especially at the initial delivery of the FFR – a large increase in both the power transfer through L29-26 and $\Delta\delta_{\max}$ can be seen. This is resulting in angle stability degradation, which is consistent with the pre-established impact of providing FFR in distant generation zones. Further, a strong deterioration in *frequency nadir* can be seen compared to when the droop scheme is installed, highlighting a trade-off between frequency stability and angle stability in derivative control implementation. Furthermore, these benefits are heavily dependent upon careful consideration and design of FFR delay, failing which could lead to angle instability as previously established in Fig. 15.

Authorized licensed use limited to: FH Dortmund. Downloaded on November 22,2024 at 11:39:02 UTC from IEEE Xplore. Restrictions apply.

B. Steady State Changes in Power Transfer

The equations presented in (7) are derived based on the assumption that only one frequency containment event, either the initial power deficit or the subsequent FFR injection, occurs in a specific area at a time. For a two-area network, four combinations of power deficit and FFR locations can be drawn. Considering this and the contribution of i-th area to the steady state power imbalance, as given by (6), produces four separate equations in (10). Combining two of the equations in (10) yields the set in (7) – the steady state changes in P_S for every possible combination of power deficit and FFR locations. Specifically,

- If the power deficit occurs at the sending end area, then P_S will *decrease* compared to the pre-event conditions. The resulting steady state decrease in P_S is given by (10a)

$$\Delta P_S = \Delta P - \frac{M_S}{M_S + M_R}\Delta P \tag{10a}$$

- Conversely, if the power deficit occurs at the receiving end area, P_S will *increase* compared to the pre-event conditions. The resulting steady state increase in P_S is given by (10b)

$$\Delta P_S = \frac{M_S}{M_S + M_R}\Delta P \tag{10b}$$

- If the FFR is provided at the sending end area, P_S will *increase* compared to when no FFR is installed. The resulting steady state increase in P_S is given by (10c)

$$\Delta P_S = P_{FFR} - \frac{M_S}{M_S + M_R}P_{FFR} \tag{10c}$$

- Conversely, if the FFR is provided at the receiving end area, P_S will *decrease* compared to when no FFR is installed. The resulting steady state decrease in P_S is given by (10d)

$$\Delta P_S = \frac{M_S}{M_S + M_R}P_{FFR} \tag{10d}$$

Combining (10a) and (10c) yields (7a), combining (10a) and (10d) yields (7b), combining (10b) and (10c) yields (7c), and, combining (10b) and (10d) yields (7d).

C. Impact of PLL Settings

A further study is completed to demonstrate that the dynamics of the PLL associated with the FFR control make a negligible difference to the results obtained in the paper – providing that a low-bandwidth PLL is used and that the BESSs are connected to a strong AC grid. Again, the modified IEEE 39-bus system (shown in Fig. 6) is used as the test network, picking up the *Base case* scenario setups given in Table II.

In all simulations presented in the main body of the paper, the FFR control PLLs are tuned with a fixed bandwidth (ω_B) of 15 Hz and a damping factor (ζ) of 0.707. To study the impact of the PLL bandwidth on the results obtained, ten possible bandwidths ranging from 5 to 100 Hz are examined, with ζ remaining unchanged. The power deficit is always applied at bus 39. The FFR provision is always delayed by 50 ms to isolate the potential instability that may be attributed to PLL rather than longer FFR delays. To assess the PLL performance under various short-circuit ratio (SCR) conditions, simulations are performed for the three possible FFR provision regions. Focus is paid to the estimated frequency signal output from the PLL (f_{PLL}) during frequency containment events. Fig. 17 displays the signals f_{PLL} at buses 39, 20, and 29.

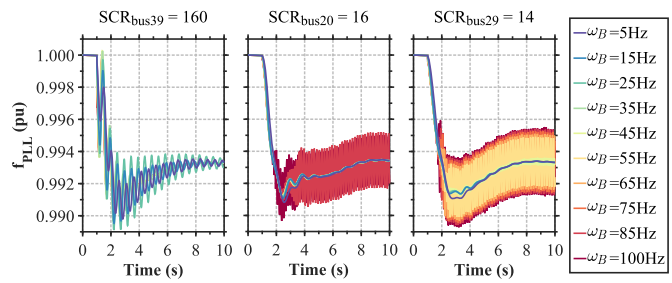

Fig. 17. PLL performance at varying bandwidths under various SCR conditions.

Low-bandwidth PLL systems (less than 50 Hz) consistently provide satisfactory performance – the PLL reacts reasonably quickly to changes in local frequency without loss of tracking. A 5 Hz bandwidth may result in a slower response, but the difference in f_{PLL} is minimal (up to 5×10^{-4} pu). As the bandwidth increases, the PLL reacts quicker, but at very high bandwidths it starts to experience hunting behavior, failing to stabilize as the input changes. This is true with lower SCR conditions (buses 20 and 29). These results are consistent with the existing literature, such as [5] and [36], which suggests that low-bandwidth PLLs are typically desired for FFR control purposes, whereas higher bandwidths can lead to unwanted or excessive operation. Considering the judicious choice of a 15 Hz PLL bandwidth and the high SCR at the BESS connection points, the PLL dynamics have a negligible impact on the results that have been presented in the paper.

D. Analytical Expression of Power Angle Curve

In (11) $Y_{12} = |Y_{12}|\angle\theta_{12}$, $Y_{13} = |Y_{13}|\angle\theta_{13}$, with notation consistent with Fig. 2(b). Recognizing the system is purely reactive, $|E'|^2 G_{11} = 0$, and $\theta_{12} = \pi/2$.

$$\begin{aligned} P_{G1} &= |E'|^2 G_{11} + |E'|\,|V_A|\,|Y_{12}|\,cos\,(\delta - \beta - \theta_{12}) \\ &\quad + |E'|\,|V_B|\,|Y_{13}|\,cos\,(\delta - \theta_{13}) \\ &= |E'|\,|V_A|\,|Y_{12}|\,cos\,(\delta - \beta - \pi/2) \\ &= \frac{|E'|\,|V_A|}{X'_d} sin\,(\delta - \beta) \end{aligned} \tag{11}$$

Acknowledgment

For the purpose of open access, the author has applied a Creative Commons Attribution (CC BY) licence to any Author Accepted Manuscript version arising.

References

[1] H. Karbouj, Z. H. Rather, F. Damian, and H. W. Qazi, "Non-synchronous fast frequency reserves in renewable energy integrated power systems: A critical review," *Int. J. Electr. Power Energy Syst.*, vol. 106, pp. 488–501, Mar. 2019.

Authorized licensed use limited to: FH Dortmund. Downloaded on November 22,2024 at 11:39:02 UTC from IEEE Xplore. Restrictions apply.

[2] J. Fradley, R. Preece, and M. Barnes, "VSC-HVDC for frequency support (a review)," in *Proc. 13th IET Conf. AC DC Power Transmiss.*, 2017, pp. 1–6.
[3] P. Kundur, *Power System Stability and Control*. New York, NY, USA: McGraw-Hill, Inc., 1994.
[4] M. F. M. Arani and E. F. El-Saadany, "Implementing virtual inertia in DFIG-based wind power generation," *IEEE Trans. Power Syst.*, vol. 28, no. 2, pp. 1373–1384, May 2013.
[5] J. Ma, Y. Qiu, Y. Li, W. Zhang, Z. Song, and J. S. Thorp, "Research on the impact of DFIG virtual inertia control on power system small-signal stability considering the phase-locked loop," *IEEE Trans. Power Syst.*, vol. 32, no. 3, pp. 2094–2105, May 2017.
[6] W. Du, Q. Fu, and H. F. Wang, "Power system small-signal angular stability affected by virtual synchronous generators," *IEEE Trans. Power Syst.*, vol. 34, no. 4, pp. 3209–3219, Jul. 2019.
[7] B. K. Poolla, S. Bolognani, and F. Dörfler, "Optimal placement of virtual inertia in power grids," *IEEE Trans. Automat. Contr.*, vol. 62, no. 12, pp. 6209–6220, Dec. 2017.
[8] B. K. Poolla, D. Groß, and F. Dörfler, "Placement and implementation of grid-forming and grid-following virtual inertia and fast frequency response," *IEEE Trans. Power Syst.*, vol. 34, no. 4, pp. 3035–3046, Jul. 2019.
[9] C. Yang, L. Huang, H. Xin, and P. Ju, "Placing grid-forming converters to enhance small signal stability of PLL-Integrated power systems," *IEEE Trans. Power Syst.*, vol. 36, no. 4, pp. 3563–3573, Jul. 2021.
[10] A. Venkatraman, U. Markovic, D. Shchetinin, E. Vrettos, P. Aristidou, and G. Hug, "Improving dynamic performance of low-inertia systems through eigensensitivity optimization," *IEEE Trans. Power Syst.*, vol. 36, no. 5, pp. 4075–4088, Sep. 2021.
[11] J. Liu, Y. Miura, H. Bevrani, and T. Ise, "Enhanced virtual synchronous generator control for parallel inverters in microgrids," *IEEE Trans. Smart Grid.*, vol. 8, no. 5, pp. 2268–2277, Sep. 2017.
[12] E. Hammad, A. Farraj, and D. Kundur, "On effective virtual inertia of storage-based distributed control for transient stability," *IEEE Trans. Smart Grid*, vol. 10, no. 1, pp. 327–336, Jan. 2019.
[13] K. Shi, W. Song, H. Ge, P. Xu, Y. Yang, and F. Blaabjerg, "Transient analysis of microgrids with parallel synchronous generators and virtual synchronous generators," *IEEE Trans. Energy Convers.*, vol. 35, no. 1, pp. 95–105, Mar. 2020.
[14] X. Zhang, H. Liu, Y. Fu, and Y. Li, "Virtual shaft control of DFIG-based wind turbines for power oscillation suppression," *IEEE Trans. Sustain. Energy*, vol. 35, no. 4, pp. 2316–2330, Oct. 2022.
[15] J. Fradley, R. Preece, and M. Barnes, "Adaptive fast frequency response for power electronic connected energy sources," in *Proc. IEEE Milan PowerTech*, 2019, pp. 1–6.
[16] S. Asvapoositkul, J. Fradley, and R. Preece, "Incorporation of active power ancillary services into VSC-HVDC connected energy sources," *Electr. Power Syst. Res.*, vol. 189, Dec. 2020, Art. no. 106769.
[17] G. Misyris, D. Ramasubramanian, P. Mitra, and V. Singhvi, "Locational aspect of fast frequency reserves in low-inertia systems–control performance analysis," in *Proc. 11th Bulk Power Syst. Dyn. Control Symp.*, 2022, pp. 1–7.
[18] P. Wall et al., "Smart frequency control for the future GB power system," in *Proc. IEEE PES Innov. Smart Grid Technol. Conf. Europe*, 2016, pp. 1–6.
[19] D. Wilson et al., *Advances in Wide Area Monitoring and Control to address Emerging Requirements related to Inertia, Stability and Power Transfer in the GB Power System*, Paris, France: CIGRE, Sess. Materials, Ref. C2-208_2016, 2016.
[20] Q. Hong et al., "Design and validation of a wide area monitoring and control system for fast frequency response," *IEEE Trans. Smart Grid*, vol. 11, no. 4, pp. 3394–3404, Jul. 2020.
[21] E. Ekomwenrenren, Z. Tang, J. W. Simpson-Porco, E. Farantatos, M. Patel, and H. Hooshyar, "Hierarchical coordinated fast frequency control using inverter-based resources," *IEEE Trans. Power Syst.*, vol. 36, no. 6, pp. 4992–5005, Nov. 2021.
[22] L. Meng et al., "Fast Frequency Response from Energy Storage Systems–A Review of Grid Standards, Projects and Technical Issues," *IEEE Trans. Smart Grid.*, vol. 11, no. 2, pp. 1566–1581, Mar. 2020.
[23] JWG C4/C6.35/CIRED, "Modelling of inverter-based generation for power system dynamic studies," Tech. Brochure, Ref. 727, CIGRE, May, 2018.
[24] J. Machowski, J. Bialek, and J. Bumby, *Power System Dynamics: Stability and Control*. U.K.: John Wiley & Sons, Inc., 2020.
[25] "Phase measurement device," in *DIgSILENT PowerFactor Technical Reference Documentation*, DIgSILENT GmbH, 2020.
[26] Australia Energy Market Operator, "Fast frequency response implementation options," Co. Report, Apr., 2021.
[27] P. V. Brogan, R. J. Best, D. J. Morrow, K. McKinley, and M. L. Kubik, "Effect of BESS response on frequency and RoCof during underfrequency transients," *IEEE Trans. Power Syst.*, vol. 34, no. 1, pp. 575–583, Jan. 2019.
[28] I. Martínez-Sanz, B. Chaudhuri, A. Junyent-Ferré, V. Trovato, and G. Strbac, "Distributed versus concentrated rapid frequency response provision in future great britain system," in *Proc. IEEE Power Energy Soc. Gen. Meeting*, 2016, pp. 1–5.
[29] National Grid ESO, New Dynamic Services (DC/DM/DR), 2020. [Online]. Available: https://www.nationalgrideso.com/industry-information/balancing-services/frequency-response-services/new-dynamic-services-dcdmdr
[30] J. D. Morales, J. V. Milanović, and P. N. Papadopoulos, "Analysis of angular threshold criteria for transient instability identification in uncertain power systems," in *Proc. IEEE Milan PowerTech*, 2019, pp. 1–6.
[31] EirGrid/SONI, "DS3 system services protocol – regulated arrangements," Co. Report, Oct. 2020.
[32] EirGrid and SONI, Operational policy roadmap 2022-2023, Co. Report, Jun. 2022.
[33] Australia Energy Market Operator, "Final report – queensland and south Australia system separation on 25 Aug. 2018," Co. Report, Jan. 2019.
[34] S Asvapoositkul, "Data-driven small-signal stability assessment and preventive control in low inertia power systems," Ph.D. dissertation, Univ. Manchester, Manchester, U.K., 2021.
[35] Z. Zhang, S. Asvapoositkul, and R. Preece, "Impact of fast frequency response on power system transient stability," in *Proc. 17th IET Conf. AC DC Power Transmiss.*, 2021, pp. 13–18.
[36] B. Vega, C. Rahmann, R. Álvarez, and V. Vittal, "Determination of control requirements to impose on CIG for ensuring frequency stability of low inertia power systems," *IEEE Access*, vol. 10, pp. 44891–44908, 2022.

Zaichun Zhang (Student Member, IEEE) received the B.Eng. degree from Northeast Electric Power University, Jilin, China, in 2017, and the M.Sc. degree in 2019, from the University of Manchester, Manchester, U.K., where he is currently working toward the Ph.D. degree. His research focuses on the stability of low inertia power systems.

Robin Preece (Senior Member, IEEE) received the B.Eng. and Ph.D. degrees from The University of Manchester, Manchester, U.K. He is currently a Reader in future power systems with the Department of Electrical and Electronic Engineering, The University of Manchester, where he has been an academic since July 2014. His research interests focus on the stability and operation of future power systems.

Authorized licensed use limited to: FH Dortmund. Downloaded on November 22,2024 at 11:39:02 UTC from IEEE Xplore. Restrictions apply.